PCCP
Physical Chemistry Chemical Physics

Accepted Manuscript

This article can be cited before page numbers have been issued, to do this please use: J. Chen, S. Guo, D. Lin, Z. Nie, C. Huang, K. Hu, C. Wang, F. Zhang, W. Zhao and W. Zhang, *Phys. Chem. Chem. Phys.*, 2021, DOI: 10.1039/D1CP00250C.

ROYAL SOCIETY OF CHEMISTRY

rsc.li/pccp

View Article Online
DOI: 10.1039/D1CP00250C

ARTICLE

Received 00th January 20xx,
Accepted 00th January 20xx

DOI: 10.1039/x0xx00000x

Ultrafast nonequilibrium dynamic process of separate electron and hole during exciton formation in few-layer tungsten disulfide†

Junjie Chen, ‡ [a] Sen Guo, ‡ [a] Dabin Lin,[a] Zhaogang Nie,*[a] Chung-Che Huang,[b] Kaige Hu,[a] Cheng Wang,[a] Fangteng Zhang [a] Weiren Zhao [a] and Wenchun Zhang [c]

Femtosecond transient absorption spectroscopy has been employed to unravel separate initial nonequilibrium dynamic process of photo-injected electrons and holes during the formation process of the lowest excitons at the K-valley in few-layer tungsten disulfide. Charge carrier thermalization and cooling as well as concomitant many-body effects on the exciton resonances are distinguished. The thermalization of holes is observed to be faster than that of electrons. Both of them proceed predominantly via carrier-carrier scattering, as evidenced by the observed dependence of the thermalization time on pump fluences. The fluence dependent time constants also suggest that the subsequent cooling for electrons is probably dominated by acoustic phonons, whereas for holes it is mostly controlled by LO phonons. An extremely fast red- and blue-shift crossover followed by a slow blue-shift of exciton resonance was observed in temporal evolution of exciton resonances by resonant exciton A excitations. The rapid red-shift could be due to the strong screening of the Coulomb interaction between quasi-free charge carriers in electron-hole plasma. The subsequent slow blue-shift is the net result of the competitions among many-body effects in the hot-exciton cooling process. Our findings elucidate the carrier-selective ultrafast dynamics and their many-body effects, underpining new possibilities for developing optoelectronic devices based on transport properties of single type of carriers.

Introduction

Two-dimensional (2D) transition metal dichalcogenides (TMDs) with atomically thin structures are currently attracting significant interests in both fundamental physics and many promising applications such as light emitters,[1,2] photodetectors/sensors,[3,4] valleytronics,[5–8] optical interconnects[9] and excitonic lasers,[10,11] due to their uniquely controllable properties.[12–14] The quantum mechanical confinement and reduced dielectric screening in these atomically thin materials result in enhanced Coulomb interactions between electron and hole,[15,16] which lead to strong excitonic effects that dominate their optical and electronic responses.[12,15–17] Significant progress has been made in understanding the exciton dynamics, for example, exciton recombination,[18,19] many-body interaction and rapid scattering among excitons,[23–28] charge transfer and interlayer excitons in hetorostructures.[29–36] Despite the extensive efforts, the exciton formation as one of the key processes to determine the excitonic effect is still yet to be understood. The exciton formation occurs immediately following the photoexcitation and thus plays a crucial role for subsequent exciton decays. Understanding the exciton formation dynamics is consequently essential for improving the optical and electronic functionalities of 2D-TMD-based devices.

So far, several optical pump–probe studies via above-resonant optical excitations have reported characteristic times on subpicosecond (sub-ps) time-scales for the formation of the lowest exciton (exciton A, X_A, see Fig. 1(a)) at the K-valley in 2D-TMDs, and have further verified that the formation time linearly increases with excitation photon energy.[37–39] A recent experiment evidenced that not all of the photogenerated charge carriers form excitons on a sub-ps time scale, indicative of a nonequilibrium state of the photoexcited electron–hole system.[39] Despite a few studies above, the dynamic picture of exciton formation is still unclear. Firstly, the early nonequilibrium free (or quasi-free) carrier distributions in principle require many carrier-carrier and carrier-phonon scatterings in the relaxation toward their respective band minima before the formation of the lowest exciton phase.[40–42] However, a targeted discussion on the carrier scatterings during the exciton formation is still locking. Secondly, the exciton formation is a process in which the photoinjected carriers, including electrons and holes, evolve from a fermionic plasma of unbound carriers with extremely high temperatures to a bosonic exciton phase associated with low temperatures due to a large binding energy. Thus the

[a] School of Physics and Optoelectronic Engineering, Guangdong University of Technology, Guangzhou 510006, Guangdong, China. *Email: zgnie@gdut.edu.cn
[b] Optoelectronics Research Centre, University of Southampton, Southampton SO17 1BJ, United Kingdom
[c] College of Traditional Chinese Medicine, Jiangxi University of Traditional Chinese Medicine, Nanchang 33004, China
† Supplementary Information (ESI) available. See DOI: 10.1039/x0xx00000x
‡ These two authors contributed equally.

unbound quasi-free electrons and holes should play an important role during the formation process. However, the experiments above were all focused on exciton dynamics or combined dynamics of electrons and holes, [37–39] rather than individual dynamics of single type of carriers. Since the effective mass of electron and hole in semiconductors are usually different,[43–45] there should be obvious differences in the scattering probability and relaxation rate between them. In addition, many-body effects, such as band-gap renormalization (BGR), Pauli blocking and Coulomb screening, in a fermionic plasma of unbound carriers should be different from those in bosonic exciton gas, which are more or less neutral particles.[46] This inevitably leads to the difference of response time between devices based on electrons and holes, respectively. So far, there is still limited insight into the sub-ps time scales during the exciton formation in 2D-TMDs. Therefore, it is highly desirable to present a detailed dynamical description of how charge carriers evolve after photo-injection, for example, to describe how highly energetic nonequilibrium electrons and holes relax into quasi-equilibrium carrier distributions and how the many-body effects between carriers affect the exciton resonance and band-gap during the exciton formation.

As one of the most important TMDs, the carrier dynamics[13,29] and many-body effects[23–26] in mono- and few-layer tungsten disulfide (WS_2) have attracted significant interests in recent years. Compared to their monolayer counterparts, few-layer TMDs have many notable superiorities such as higher electron mobility, stronger photon absorption ability and larger optical density of states.[47] For example, the few-layer WS_2 has been demonstrated to be an excellent channel material with good electron mobilities of 234 $cm^2 V^{-1} s^{-1}$ and on/off ratios exceeding 10^8 for the making of high performance field-effect transistors, required for both energy saving and high power electronics applications.[48] In this present work, we report the use of femtosecond transient absorption spectroscopy to address separately the ultrafast nonequilibrium dynamics of electrons and holes in the formation process of the lowest X_A at the K-valley in few-layer WS_2, used as an example. A nondegenerate pump-probe scheme is used to isolate separately the nonequilibrium dynamics, including carrier thermalization and cooling processes, of electrons and holes as well as the concurrent exciton resonance evolution that are controlled by intense many-body interactions among carriers during the exciton formation process. It should be noted that, as the carrier dynamics at the K-valley also dominates the photoelectric response in mono-layer TMDs,[13,29] our study is also significant for mono-layer applications.

Experimental section

Sample preparation

The few-layer WS_2 film sample was prepared by Van der Waals epitaxy (VdWE) process.[49–51] In this process, WCl_6 (99.9% pure from Sigma-Aldrich) was kept in a bubbler at room temperature, and WCl_6 vapour was delivered by argon gas through a mass flow controller (MFC) to the VdWE quartz reaction tube. The reactive gas, H_2S, was delivered through second MFC and then mixed with another argon gas through a third MFC. The argon gas flow rate for delivering WCl_6 precursor was typically set at 300 standard cubic centimeters per minute (sccm) and H_2S/Ar gas mixture were typically set at 50 sccm and 300 sccm respectively. The whole system was connected to a chemical resistant pump (Vacuubrand MV 10C NT Vario) with a pressure controller set at 30 mBar for the entire deposition process. With this VdWE apparatus, uniform large-scale multilayer WS_2 were epitaxially grown on fused silica substrates (more than 20mm × 20mm) at the furnace temperature set at 900 °C. The Raman spectrum of the sample, as shown in Fig. S1(e) in the Electronic Supplementary Material (ESM), indicates that the sample is four-layer.[52]

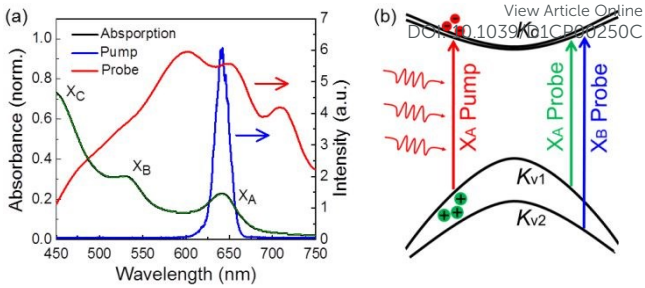

Fig. 1 (a) UV/visible absorption spectrum of the five-layer WS_2 sample collected at 300 K (black line). The green line is the fitting result by a three-Gaussian superimposed on a cubic polynomial function. The X_A and X_B transitions are centered at 640 and 531 nm, respectively. The narrowband (blue line) and broadband (red line) laser spectra employed for pump and probe pulses, respectively, are shown together. (b) Schematic illustration for the band-selective probing of ultrafast electron and hole relaxation dynamics in WS_2. Following resonant excitation of the X_A transition, the X_B probe interrogates the electron dynamics at K_c. With knowledge of the electron dynamics, the hole dynamics at K_{v1} can be extracted from the X_A probe signal, which reflects both electron and hole dynamics.

Transient absorption spectroscopy

In the ΔA measurements, an 800 nm output pulse laser (1 kHz repetition rate, 35 fs pulse width) from an amplified Ti:sapphire laser system (Solstice Ace35F1K HP, Spectra Physics) was split into two paths. One beam was sent to an optical parametric amplifier (Spectra-Physics TOPAS) to generate narrowband pump pulse, which wavelength can be tuned within 250–1100 nm. The second beam was focused into a noble gas filled hollow-core-fiber, followed by a chirped-mirror compressor (UltraFast Innovations, Design PC1332), to generate sub-10 fs broadband pulse within ~480–950 nm. A part of the broadband spectrum is shown in Fig. 1(a). A small part of the broadband pulse was separated from the sub-10 fs pulse to be used as the probe pulse. A second-order intensity cross-correlation between the narrowband pump and broadband probe pulses, performed in a 10 μm thick BBO crystal located at the position of the sample target, reveals a time resolution of 65 fs fwhm for the apparatus (Fig. S2(a) in the ESM). The sub-10 fs broadband pulse duration is also verified by the cross-correlation measurement (Fig. S2(b) in the ESM). The pump and probe beams are both linearly polarized and perpendicular to each other to minimize the coherent artifacts in the ΔA signals, which can be further suppressed by singular-value decomposition of the 2D probe energy-time delay data set. The transmitted probe beam is spectrally dispersed in a 300 mm spectrograph and detected by a 1024-element linear array detector, with a read-out rate of 1 kHz and synchronized to a 500 Hz optical chopper positioned in the path of pump beam.

The transient absorption signal was obtained by measuring the differential absorbance spectra $\Delta A = -\log_{10}(1+\Delta T/T)$, where $\Delta T/T = (T_{on}-T_{off})/T_{off}$, T_{on} and T_{off} are the intensity of the transmitted probe light passing through the sample in both the presence and absence of the pump excitation. The spot size of pump and probe on the sample are 420 μm and 190 μm, respectively. A computer-controlled, piezo-driven high precision translation stage (Physik Instrumente) incorporated with a long travel range motorized stage (Newport) was placed in the pump beam arm to generate a time delay between pump and probe pulses with 2 fs time delay precision. We estimate the excited carrier density (0.7–3.9×10^{13} cm^{-2}) from the measured incident pump fluence and the absorbed laser spectra of the sample at the excitation wavelength. The detailed methods for ultrashort pulse generation and carrier density estimation were described in our previous work.[41] Compared to previous reports on exciton formation,[37–39] in which the carrier density is in a low regime (~1×10^{12} cm^{-2}), the carrier density in this work is in a high density regime, so as to increase the initial quasi-free carrier density of the electron-hole plasma and to enhance the many-body effects in carrier dynamics. All measurements are performed at 300 K. Excitation pump fluence-dependence measurement was performed to verify that photoexcitation of the sample occurs in the one-photon regime (Fig. S3 in the ESM).

Results and discussions

The stead-state absorption spectrum of the sample at 300 K is shown in Fig. 1(a). The pump laser spectrum peaking at 640 nm for X_A resonant excitation and a part of broadband probe laser spectrum in a range of 450–750 nm are shown together with the absorption for transient differential absorption (ΔA) signal detection. The absorption contains three peaks assigned to X_A, X_B, and X_C excitonic transitions.[17,33] The absorption can be fit to three Gaussian functions superimposed on a cubic polynomial. The cubic polynomial component and the three Gaussian curves for the fitting are shown in Figs. S1(a–c) in the ESM. The two lowest excitons X_A and X_B originate from transitions between the spin–orbit split levels in the valence band and conduction band at the K-valley of the Brillouin zone.[17] A nondegenerate pump-probe scheme is used to isolate the electron and hole dynamics, as demonstrated in Fig. 1(b), which is similar to that used early in optical pump-probe studies of GaAs to measure the electron dynamics independently.[54,55] To isolate the electron dynamics, a narrowband laser pulse as the pump pulse resonantly excites the electrons from the spin-split lower valence band K_{v1} to the lowest conduction band K_c due to X_A transition, while a broadband pulse as the probe that spans the absorption of X_A and X_B transitions is used to collect the ΔA signal. The pump energy is chosen low enough to promote electrons from the K_{v1} valence bands to K_c conduction bands (Fig. S1(d) in the ESM). Different from few-layer MoS_2,[41] the transition bands of X_A and X_B are separated very well at the K-valley,[38] as shown in Fig. S1(c) in the ESM. In this case, almost no holes are generated in the spin-split higher valence band K_{v2} band. Note that the spin-orbit splitting of lowest energy states (K_{c1} and K_{c2}) at conduction band is ~200 cm^{-1},[56] which is much smaller than the frequencies of the strongest phonons(~300–450 cm^{-1}, see Fig. S1e)

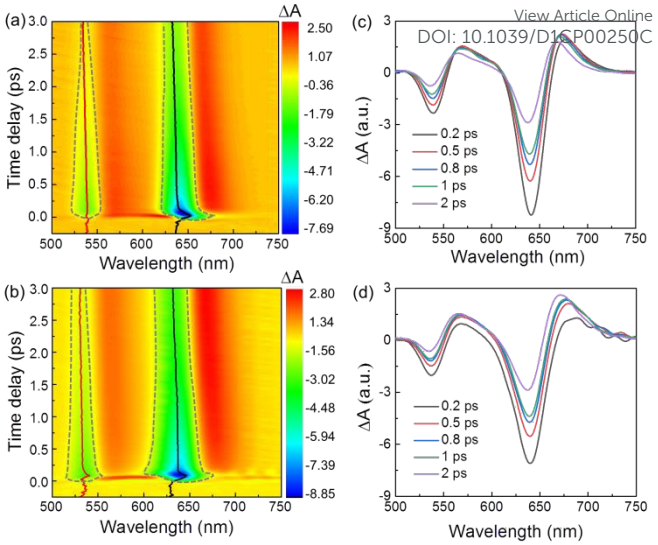

Fig. 2 Differential absorption ΔA spectra collected as a function of time delay following photoexcitation of the WS_2 sample with pump wavelengths at 640 nm (a,c) and 625 nm (b,d). The dotted gray lines and the solid lines in (a,b) are respectively the contour lines and the first moment traces as eye guides to show the peak shift of X_A and X_B resonances. Pump fluences of 0.24 mJ/cm^2 and 0.51 mJ/cm^2 are respectively used for 640 nm and 625 nm excitations. The sample temperature is 300 K.

in WS_2. In principle, the electrons can easily traverse these two states, mediated by phonons in the carrier relaxation process. Thus in this work we assume the X_A and X_B transitions share the same lowest state (K_c), as shown in Fig. 1b. After laser excitation, there could also be a possibility that the electrons in the higher energy state K_{v2} relax to the lower energy state K_{v1}, leaving holes in the K_{v2}. However, the energy separation of K_{v1} and K_{v2} in the valence band is ~3500 cm^{-1},[56] which is around ten times larger than the strongest phonon frequencies, leading to a much slower non-radiative relaxation than that in K_c. According to this hypothesis, the temporal evolution of the ΔA signal between K_{v2} and K_c is dominately sensitive to electron distribution in K_c in the initial exciton formation process. Since the X_A and X_B transitions include the same electron dynamics at K_c, the hole dynamics at K_{v1} can then be recovered from the temporal evolution of the X_A transition, which bear contributions from both electron and hole dynamics.

Figs. 2(a) and (b) present the 2D plots of ΔA spectra obtained by excitations of X_A at 640 nm and 625 nm respectively, where the colour scale, the horizontal axis and the vertical axis represent the magnitude of ΔA, the probe wavelength and the pump–probe time delay, respectively. The pump spectra peaking at 625 nm is presented in Fig. S1(e), which is on the blue side of X_A absorption. Figs. 2(c) and (d) further show several ΔA spectra recorded up to 3 ps to demonstrate the general spectral features of ΔA. According to the steady-state absorption spectrum shown in Fig. 1(a) and Fig. S1(a), the negative ΔA bands at 640 nm and 531 nm reflect ground state bleachings (GSB) of the X_A and X_B transitions. The positive ΔA features are induced absorptions, which can be attributed to carrier-induced peak broadening or transitions to higher energy levels.[38] The dotted curves and the solid lines superimposed on the 2D plots in Figs. 2(a) and (b) are contour lines and first moment traces of the two GSBs, which will be used later to discuss the many-body effects on excitonic resonances.

View Article Online
DOI: 10.1039/D1CP00250C

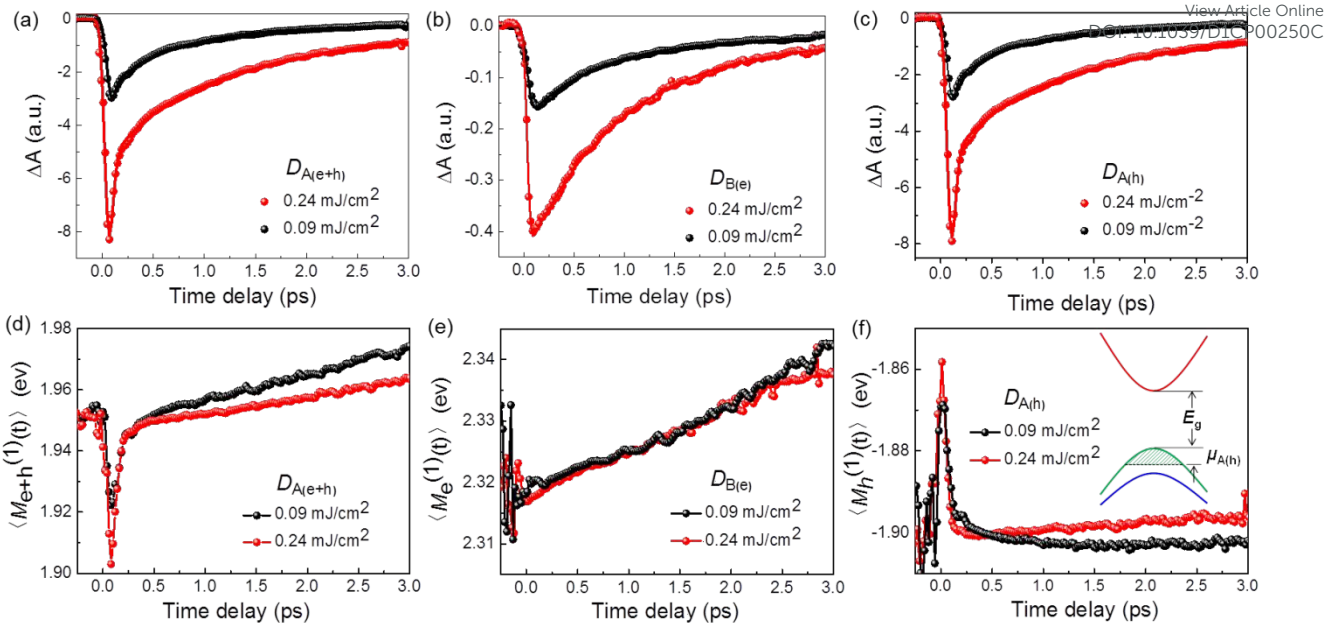

Fig. 3 (a) $D_{A(e+h)}$ peak traces obtained at 640 nm for X_A transition, (b) $D_{B(e)}$ peak traces at 530 nm for X_B transition and (c) $D_{A(h)}$ peak traces, obtained at two different pump fluences under resonant X_A excitation at 640 nm. The solid lines in (a–c) are the fitting due to the convolution of a mono- or bi-exponential decay function with the Gaussian IRF of the experiment (see Fig. S2(a) in the ESM). (d) $\langle M_{e+h}^{(1)}(t)\rangle$ traces of $D_{A(e+h)}$ for X_A transition, (e) $\langle M_e^{(1)}(t)\rangle$ traces of $D_{A(e)}$ peaking for X_B transition and (f) $\langle M_h^{(1)}(t)\rangle$ traces, obtained at two different pump fluences under resonant X_A excitations at 640 nm.

The dynamics of X_A ($D_{A(e+h)}$), including the combined contributions from electron and hole (electrons in K_c and holes in K_{v1}), reflects the formation process of hot excitons and their subsequent cooling process toward their band edges. Here, a hot exciton is referring to a state where an electron is weakly bound with a hole and its energy and temperature is much higher than the tightly bound exciton at the bottom of the band edge. As mentioned above, the dynamics of X_B ($D_{B(e)}$) originated from pure electrons in K_c. If we take only into account the contribution of population difference in ΔA. Then with knowledge of the electron dynamics, the hole dynamics $D_{A(h)}$ can be recovered from $D_{A(e+h)}$ by the difference signal calcualtion, $D_{A(h)} = D_{A(e+h)} - D_{B(e)}$.

The time traces probed at the GSB peaks of the X_A and X_B transitions, named as peak traces, are chosen to describe the carrier relaxation dynamics. The peak traces of $D_{A(e+h)}$ at 640 nm and those of $D_{B(e)}$ at 531 nm are shown in Figs. 3(a) and (b), respectively, at two pump fluences. The pump fluences are 0.09 mJ/cm^2 and 0.30 mJ/cm^2, corresponding to single-layer carrier densities in a range of 0.7–2.3×10^{13} cm^{-2}. The calculated $D_{A(h)}$ is plotted in Fig. 3(c). The evolution of $D_{A(e+h)}$, which reflects the combined dynamics of electrons and holes, exhibits a similar behavior to $D_{A(h)}$. Both of them appear to be biphasic in the time scale of our measurements, which spans <100 fs to 3 ps, whereas $D_{B(e)}$ exhibits a monophasic profile. The similarity of $D_{A(e+h)}$ and $D_{B(e)}$ reminds us that the contribution of the early fast decay in $D_{A(e+h)}$ is mostly from $D_{A(h)}$, since $D_{B(e)}$ includes only a slow decay component. To take into account the temporal widths of the pump and probe pulses,[29] the exponential fitting was done by convoluting with the Gaussian instrument response function (IRF), as follows

$$\Delta\mathbf{A}(\lambda,t) = \boldsymbol{y_0}(\lambda) + \mathrm{IRF}(t) * \left\{\mathbf{S(t)} \times \left[\Delta\mathbf{A_0}(\lambda) + \Delta\mathbf{A}(\lambda)\boldsymbol{e}^{-t/\tau_i}\right]\right\} \quad (1)$$

where λ is the peak wavelength, t is the time delay, $y_0(\lambda)$ is the overall offset at the peak wavelength position, IRF(t) is the instrument response function (IRF), S(t) is the step function, $\Delta A_0(\lambda)$ is the offset after time-zero, reflecting the ΔA spectrum in the limit of large time delays, and ΔA(λ) is the ΔA signal at λ position that decays exponentially with the time constant τ_i (i = 1, 2), corresponding to mono- or bi-exponential functions. The IRF is obtained by the intensity cross-correlation trace of pump and probe pulses (Fig. S2(a) in the ESM). The returned fitting results are listed in Table 1. Two time constants for the fast and slow processes in $D_{A(e+h)}$ ($D_{A(h)}$) are denoted as $\tau_{f(e+h)}$ ($\tau_{f(h)}$) and $\tau_{s(e+h)}$ ($\tau_{s(h)}$), respectively. For $D_{B(e)}$, only a time constant $\tau_{s(e)}$ due to the slow process was obtained. It is seen that $\tau_{f(e+h)}$ and $\tau_{f(h)}$ both decrease significantly with increasing pump fluences and they are close to each other at the same pump fluences. Different from the fast decay in $D_{A(h)}$ (or $D_{A(e+h)}$), it is interesting that the dependence of $\tau_{s(e)}$ and $\tau_{s(h)}$ ($\tau_{s(e+h)}$) (see Table 1) exhibit opposite trends in their fluence dependence: $\tau_{s(e)}$ decreases with pump fluence, whereas $\tau_{s(h)}$ ($\tau_{s(e+h)}$) increases.

The schematic illustration of electron and hole dynamics in the K-valley during the formation of the lowest excitons is presented in Fig. 4. In principle, immediately following the laser excitation, electron-hole plasma should be generated with a nonequilibrium

Table 1 Exponential fitting results of peak traces due to $D_{A(e+h)}$, $D_{A(e)}$ and $D_{A(h)}$ dynamics as a function of pump fluence under resonant X_A excitations at 640 nm. The pump fluences are from 0.09 mJ/cm^2 to 0.30 mJ/cm^2, corresponding to single-layer carrier densities in a range of 0.7–2.3×10^{13} cm^{-2}.

Fluence	$\tau_{f(e+h)}$ (fs)	$\tau_{s(e+h)}$ (fs)	$\tau_{s(e)}$ (fs)	$\tau_{f(h)}$ (fs)	$\tau_{s(h)}$ (fs)
0.09 mJ/cm^{-2}	60 ± 5	790 ± 10	930 ± 10	80 ± 7	770 ± 9
0.12 mJ/cm^{-2}	50 ± 9	830 ± 9	847 ± 9	60 ± 9	850 ± 11
0.24 mJ/cm^{-2}	20 ± 5	990 ± 9	749 ± 11	19 ± 5	953 ± 10
0.30 mJ/cm^{-2}	15 ± 3	1010 ± 8	705 ± 8	16 ± 5	1000 ± 10

(or non-thermal) distribution and with a relatively localized density in momentum space. Similar situations were also reported in multilayer MoS_2[41] and GdAs/AlGaAs nanowires.[57] As the exciton wave function is composed of free carrier states in the initial time range, the band filling when charge carriers move from high to low energy states in the carrier thermalization process can alter the oscillator strength and saturate the exciton absorption in the K-valley. As the exciton wave function is composed of free carrier states in the initial time range, the band filling when charge carriers move from high to low energy states in the carrier thermalization process can alter the oscillator strength and saturate the exciton absorption in the K-valley. For example, the electrons in the conduction band reduces the absorption since the electrons occupy states from which an exciton is constructed and these final states are not available for the transition, thus resulting in a decrease of the ΔA signal,[37,41,58] as in our experiments. It was proved that the initially injected charge carriers are about twice more efficient on inducing transient absorption than excitons. [37,53] Several previous studies of exciton dynamics in 2D-TMDs have indicated that in the case of resonant excitations, the majority of excited population decays via thermalization and cooling within the first around one picosecond.[38,41,59] The evolution of the initial nonthermal distribution of carrier energies toward a hot quasiequilibrium Fermi-Dirac distribution was reported to be on a typical time scale of sub-100 fs in 2D-TMDs.[41,59] The appearance of the <100 fs fast decay component in $\tau_{f(h)}$ is thereby assigned to the thermalization of holes, while the slow processes with sub-ps time constants, $\tau_{s(e)}$ and $\tau_{s(h)}$, are respectively due to the cooling of pure electrons and holes. The $\tau_{f(e+h)}$ and $\tau_{s(e+h)}$ are thereby due to the combined dynamics of electrons and holes in thermalization and cooling process. It was reported that the carriers with nonthermal distribution randomize their momenta primarily by carrier-carrier scatterings.[41,60,61] As a result, the thermalization rate is expected to increase with pump fluence (or carrier density). This is in good agreement with our experiment results, as listed in Table 1. Note that it is difficult here to distinguish the difference of the time constants between the charge carrier thermalization and the formation of hot excitons. Their kinetic mechanisms are different. The former is due to the energy redistribution through carrier scattering, while the latter originates from the attraction of electrons and holes. Both were accomplished in an extremely short time. The measured carrier thermalization time in WS_2 is comparable to those of MoS_2,[41] and graphene,[62] which were also found to be <100 fs.

After thermalization, the probed states are governed by high-temperature carrier populations, which decreases by cooling or relaxation via intra- and inter-valley carrier-phonon scattering. The intravalley scattering releases the carrier energy by phonon emission and leads to the carrier relaxation from the higher vibrational states to the lower ones in the K valley, whereas the intervalley scattering results in the transfer of electrons and holes to the Q valley in the conduction band and Γ in the valley band, respectively.[41] As mentioned above, the fluence dependence measurements show that $\tau_{s(e+h)}$ and $\tau_{s(h)}$ are both prolonged by increasing fluence (See Table 1), while $\tau_{s(e)}$ is shortened. Analogous to the situation encountered in few-layer MoS_2,[41] the behaviors of $D_{A(e+h)}$ and $D_{A(h)}$ are consistent with the hot LO-phonon effect,

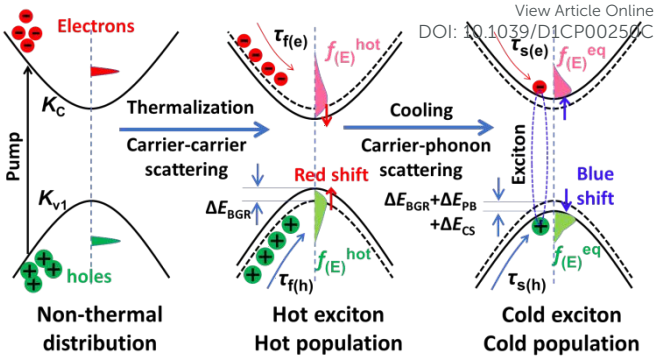

Fig. 4 Scheme of the thermalization and cooling of separated electrons and holes. The initially δ-like distribution functions are depicted for electrons in the conduction band (K_c) and holes in the valence band (K_{v1}). After thermalization via carrier-carrier scattering the electrons and holes form hot excitons and assume a hot thermal distribution, $f_{(E)}^{hot}$, in K_c and K_{v1}, respectively. When the charge carriers cooled down sufficiently to reach equilibrium with the crystal lattice via carrier-phonon scattering, the electrons and holes form cold excitons at the bottom of the energy bands and exhibit an equilibrium distribution ($f_{(E)}^{eq}$).

whereby a large LO-phonon population with high temperatures that results from high density of hot carriers impedes the carrier cooling.[63] In other words, when the LO-phonon population reaches its maximum in the carrier relaxation process, the reverse energy reabsorption from hot phonons to carrier system slows down the cooling process. Different from the LO-phonons, the acoustic phonon is assumed to be in thermal equilibrium with the lattice and the substrate, thus making them relatively insensitive to the hot phonon effect.[64] The assistance of acoustic phonons can even lead to an acceleration with increasing pump fluence via intra- and inter-valley scattering in the cooling process. Therefore, we prefer to have the competition of optical and acoustic phonons in the cooling processes of separate electrons and holes. According to the pump-fluence dependent results, we infer that the elecron cooling in K_c might be dominated by acoustic phonons, whereas the hole relaxation in K_{v1} could be controlled by LO-phonons. The subsequent exciton-exciton annihilation or Auger recombination process (not shown) is also expected to accelerate with increasing pump fluence. However, the Auger process is typically on a time scale of $\gtrsim$ 100 ps,[19,65] which is not expected to contribute significantly to the sub-ps exciton formation dynamics in this work. Note that the results obtained above are different from those in previous studies on sub-ps exciton formation with resonant X_A excitation.[37] In those experiments, the early sub-ps decay is absent when excitons are resonantly injected. This is because the photoinjected carriers are in a low carrier density regime, which results in the direct formation of resonant excitons, instead of high density free carriers with high temperatures, as in our experiments.

Also illustrated in Fig. 4, along with the non-equilibrium carrier relaxation during exciton formation, the high density of carriers in 2D-TMDs may induce various many-body effects,[23–28] resulting in the temporal modulation of the optical bandgap and also the exciton resonance peaks. First of all, the BGR effect (ΔE_{BGR}) due to non-equilibrium occupation of electron and hole states can cause the band edge to shift below the initial position of the exciton resonance. Second, Pauli blocking effect (ΔE_{PB}) arising from Pauli exclusion principle because of the fermionic nature of electrons and

holes would cause a reduction of exciton binding energy and gradually drive the onset of direct dipole transition to higher energies. Third, the carrier screening of the Coulomb interaction (or Coulomb screening, ΔE_{CS}) can also lead to a decrease of the exciton binding energy. Some other effects, such as intervalley plasmons,[66,67] are not included, since only the K-valley dynamics are involved here. The significant BGR effect and the reduction of exciton binding energy due to the latter effects, Pauli blocking and Coulomb screening, strongly modifies optical response and compete with each other, leading to shifts of exciton resonance and optical bandgaps either to higher or lower energy. The temporal evolution of exciton resonance can therefore serve as a delicate probe of the competition among the many-body effects. Carefully inspection of the contour lines in Fig. 2(a) under 640 nm excitation suggests there is an obvious early rapid red-shift in X_A resonance. Similar rapid shift appears for X_B resonance when the pump peak wavelength was tuned to be at 625 nm, as shown in Fig. 2(b). These observations indicate that there are intense many-body effects among nonequilibrium carriers. The time evolution of exciton resonance (or band structure) can be further discerned from the spectral first moment trace (soid lines in Fig. 2(a) and (b)),[41,68] defined as

$$\langle M_{e,h}^{(1)}(t)\rangle = \int_{E_i}^{E_f} E\Delta A(E,t)dE \Big/ \int_{E_i}^{E_f} \Delta A(E,t)dE \qquad (2)$$

where, t is the pump-probe time delay, E is the probe photon energy (in eV), E_i and E_f correspond to the limits of the integral, and $\Delta A(E,t)$ is the difference absorption spectra as a function of the probe photon energy. The $\langle M_{e,h}^{(1)}(t)\rangle$ traces give the evolution of energy difference between the bands which are optically coupled by the broadband probe pulse.

The calculated $\langle M_{e+h}^{(1)}(t)\rangle$, $\langle M_e^{(1)}(t)\rangle$ and $\langle M_h^{(1)}(t)\rangle$ respectively for $D_{A(e+h)}$, $D_{B(e)}$ and $D_{A(h)}$ with two different pump fluences are shown in Figs. 3(d–f). The $\langle M_h^{(1)}(t)\rangle$ is equal to the sum of the energy bandgap (E_g), obtained from the static absorption spectrum in Fig. 1(a) and Fig. S1(d), and the temporal evolution of chemical potential ($\mu_{A(h)}$) of K_{v1}. In the calculation, the bottom of conduction band is used as the reference of zero energy position. Here, the E_g is a constant and the $\mu_{A(h)}$ of K_{v1} (see the inset of Fig. 3(f)) can be modulated as a function of time by many-body effects.[69] As shown, the evolution of $\langle M_{e,h}^{(1)}(t)\rangle$ can be adequately described by two stages in chronological order. In stage I, for $\langle M_{e+h}^{(1)}(t)\rangle$ and $\langle M_h^{(1)}(t)\rangle$, the moment traces exhibit a similar initial fast red- and blue-shift crossover, starting from carrier photoinjection time point to within 200 fs. The red-shift takes place as hot carriers are injected by incident pumps and its amplitude increases slightly with increased pump fluence. Compared with the peak traces in Figs. 3(a) and (c), the rapid initial crossover appears simultaneously with the fast thermalization process in $D_{A(e+h)}$ and $D_{A(h)}$. For $\langle M_e^{(1)}(t)\rangle$, there isn't obvious initial rapid shift in stage I, as seen in Fig. 3(b).

Insight from microscopic theory reveals that the initial red-shift observed in stage I mainly arises from high-density plasma induced BGR.[21,25,26,69] The red-shift for charge carrier generation was theoretically expected in WS_2 near the insulator-metal transition, but not observed for the comparatively low excitation densities used in previous works.[21,25] Here, the Coulomb interaction due to the non-equilibrium occupation of electron and hole states is strongly screened when carrier density is in high-density regime, which is comparable to the theoretically predicted 2D Mott density in monolayer WS_2 (~1×10^{13} cm^{-2}).[46] The reduction of the repulsive Coulomb interaction between the charges of the same sign results in a decrease in the quasi-particle energy. This produces BGR, shifting the bandgap even below the initial exciton resonance peak energy. The BGR can play a dominant role in the initial thermalization process. More detailed discussions of BGR can be

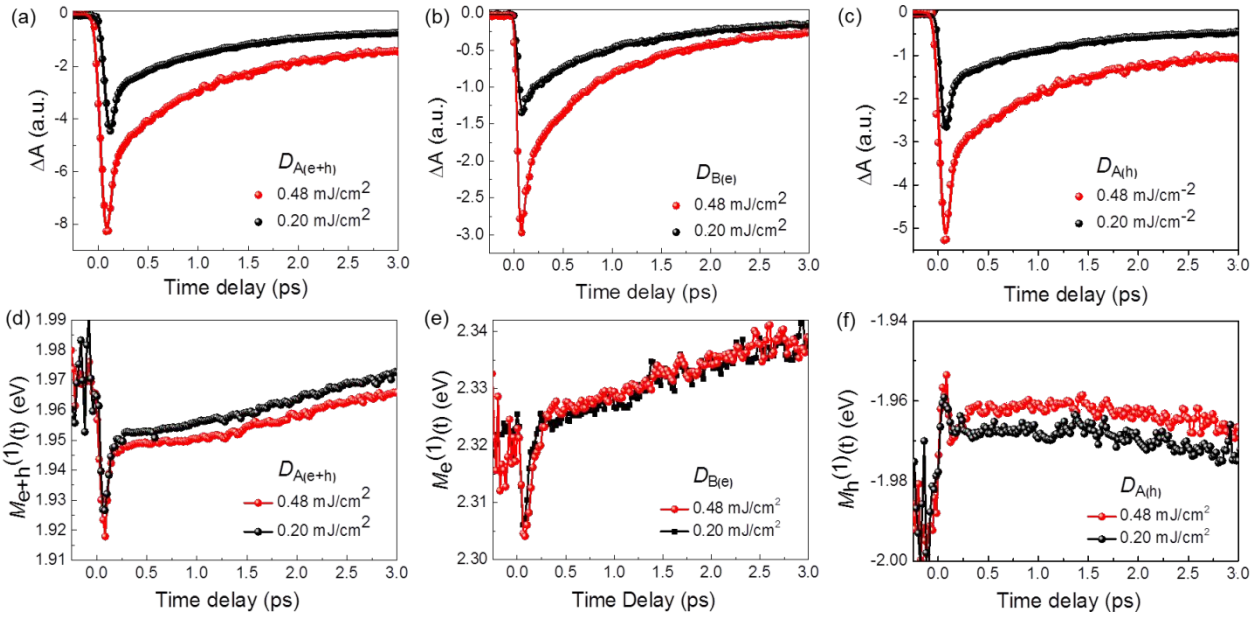

Fig. 5 (a) $D_{A(e+h)}$ peak traces for X_A transition and (b) $D_{B(e)}$ peak traces for X_B transition and (c) $D_{A(h)}$ peak traces calculated by $D_{A(e+h)}$–$D_{B(e)}$ for X_A transition, obtained at two different pump fluences under excitation of X_A transition at 625 nm. The solid lines in (a–c) are obtained by fitting the data to the convolution of a bi-exponential decay function with the Gaussian IRF of the experiment (see Fig. S2 in the ESM). (d) $\langle M_{e+h}^{(1)}(t)\rangle$ traces of $D_{A(e+h)}$ for X_A transition, (e) $\langle M_e^{(1)}(t)\rangle$ traces of $D_{A(e)}$ for X_B transition and (f) $\langle M_h^{(1)}(t)\rangle$ traces for X_A transition, obtained at two different pump fluences under X_A excitations at 625 nm.

found in Ref. 69. The slight increase of the red-shift with higher pump fluence in Figs. 3(d) and (f) indicates the intensification of the screening effect. The following rapid blue-shift reflects the recovery process of the Coulomb interaction. For the evolution of $\langle M_{e+h}^{(1)}(t)\rangle$, which reflects the combined dynamics of electrons and holes, it exhibits a similar behavior to $\langle M_h^{(1)}(t)\rangle$. The red- and blue-shift crossover in $\langle M_{e+h}^{(1)}(t)\rangle$ originates from the many-body effects of combined electrons and holes. Since there isn't obvious initial peak shifts in $\langle M_e^{(1)}(t)\rangle$, as mentioned above, the shfit-crossover in $\langle M_{e+h}^{(1)}(t)\rangle$ is most probably due to the many-body effect among holes.

In the following stage II the first moment traces exhibit similar slow blue-shifts in $\langle M_{e+h}^{(1)}(t)\rangle$, $\langle M_e^{(1)}(t)\rangle$ and $\langle M_h^{(1)}(t)\rangle$ traces. This blue-shift is actually similar to that reported for exciton dynamics in a low and intermediate density excitation regime.[21,25] In this stage, hot carriers start to fill the lowest conduction and valence band and more and more lowest excitons at band edges were created. For $\langle M_{e+h}^{(1)}(t)\rangle$, except for BGR there are usually two more effects which can affect the excitonic resonance: Pauli blocking and screening of the Coulomb interactions. Different from BGR, the latter two effects can lead to the decrease of the exciton binding energy. Incomplete compensation of these effects may produce a net peak shift of exciton resonance inducing a redshift or a blueshift.[20,21] The slow blue-shift in stage II of $\langle M_{e+h}^{(1)}(t)\rangle$ indicates that the latter two effects dominate in the competitive process. A careful comparison of $\langle M_e^{(1)}(t)\rangle$ and $\langle M_h^{(1)}(t)\rangle$ traces shows that after the early rapid blue-shift in stage I, the subsequent slow blue-shift in $\langle M_h^{(1)}(t)\rangle$ is more sluggish than that in $\langle M_e^{(1)}(t)\rangle$. Thus, by comparing $D_{A(e)}$ and $D_{B(h)}$, it is reasonable that the contribution from $\langle M_e^{(1)}(t)\rangle$ is more than $\langle M_h^{(1)}(t)\rangle$ to the slow blue shift in $\langle M_{e+h}^{(1)}(t)\rangle$. We note that although the $\langle M_e^{(1)}(t)\rangle$ at this stage still reflects the many-body effects among pure electrons, we cannot exclude the influences induced by the Coulomb constraints of electron-hole pairs due to the formation of hot excitons.

Table 2 Time constants obtained by bi-exponential fitting the peak traces due to $D_{A(e+h)}$, $D_{B(e)}$ and $D_{A(h)}$ dynamics as a function of pump fluence under X_A excitations at 625 nm. The pump fluences are from 0.16 mJ/cm^2 to 0.48 mJ/cm^2, corresponding to single-layer carrier densities in a range of 1.3–0.39×10^{13} cm^{-2}.

Fluence (mJ/cm^{-2})	$\tau_{f(e+h)}$ (fs)	$\tau_{s(e+h)}$ (fs)	$\tau_{f(e)}$ (fs)	$\tau_{s(e)}$ (fs)	$\tau_{f(h)}$ (fs)	$\tau_{s(h)}$ (fs)
0.16	24 ± 3	940 ± 7	103 ± 2	1004 ± 7	32 ± 5	866 ± 9
0.20	22 ± 3	950 ± 10	98 ± 3	980 ± 11	26 ± 8	976 ± 18
0.32	16 ± 4	961 ± 11	70 ± 5	930 ± 10	19 ± 4	980 ± 11
0.48	12 ± 5	994 ± 9	31 ± 5	863 ± 12	13 ± 6	1011 ± 25

As mentioned above, under resonant X_A excitation at 640 nm there isn't distinguishable initial thermalization process in $D_{B(e)}$ and also no early rapid red-shift in $\langle M_e^{(1)}(t)\rangle$. The pump power was further increased to inject even higher carrier density, the fast decay can really appear in $D_{B(e)}$ peak traces, but the laser power used is too high to beyond the linear dependent regime in this experiment. It was reported that in the case of excitations at higher energies than exciton resonance energy, more absorbed photons will be consumed for unbound electrons and holes.[37–39] Thus further experiments were tried with higher pump photon energy at 1.98 eV (625 nm). The narrowband pump spectrum peaking on the blue side of the X_A absorption band is shown in Fig. S1(d). Note that in this case the pump energy is a little higher than the X_A resonance energy (1.93 eV, 640 nm) and the pump laser spectrum is still in the resonant absorption range of X_A (see Fig. S1(d)). Except for higher pump photon energies, a bit higher pump fluences in the linear dependent regime were used, resulting in higher carrier densities and higher carrier temperatures. One of the corresponding 2D plots of ΔA spectra obtained by pumping at 625 nm is shown in Fig. 2(b). In contrast to Fig. 2(a), the contour line and the first moment trace due to X_B resonance band indicates obviously that the initial resonance in the early time range is distorted to the direction of lower energy. The corresponding peak traces and the first moment traces due to $D_{A(e+h)}$, $D_{B(e)}$ and $D_{A(h)}$ dynamics at two pump fluences are shown in Fig. 5. The peak traces of $D_{A(h)}$ are still calculated by $D_{A(e+h)}$–$D_{B(e)}$. Similar to $D_{A(e+h)}$, the peak traces of $D_{B(e)}$ and $D_{A(h)}$ are both biphasic and the early fast decays appear simultaneously with the initial red- and blue-shift crossovers in $\langle M_e^{(1)}(t)\rangle$ and $\langle M_h^{(1)}(t)\rangle$ traces. This is different from the phenomena under excitation at 640 nm.

The bi-exponential fitting results of $D_{A(e+h)}$, $D_{B(e)}$ and $D_{A(h)}$ peak traces are presented in Table 2. For the fast processes, $\tau_{f(e+h)}$, $\tau_{f(e)}$ and $\tau_{f(h)}$ all decrease with increasing pump fluences, exhibiting the same trends to those under 640 nm excitations (see Table 1), suggestive of carrier-carrier scattering occurring in the early carrier thermalization process. The $\tau_{f(e+h)}$ becomes shorter than those under resonant excitations at 640 nm, because the pump fluence used is higher than before. At the same pump fluence, the $\tau_{f(e)}$ is much longer than $\tau_{f(h)}$. This could because the effective mass of electrons (m_e) is smaller than that of holes (m_h),[43–46] indicative of the faster processes in $D_{A(e+h)}$ mostly associated with holes.[70] This is to some extent consitent with the first moment traces in Fig. 3(f) and Fig. 5(f), which show that the slower blue-shift process in stage II for holes is very flat in contrast to those of electrons (Fig. 3(e) and Fig. 5(e)). That is, the holes take a shorter time to go to an equilibrium state in K_{v1} than electrons in K_c after thermalization. Note that the fast decay in $D_{B(e)}$ should not be due to the electron relaxation from the photoinjected higher energy position (1.98 eV, 625 nm), because it will result in an increase of the population at the states probed or a rise (not a decay) process in the GSB peak traces at the lower energy positions (~1.93 eV, ~640 nm).

For the subsequent cooling processes, all the time constants exhibit the same trends as they do under 640 nm excitation. That is, $\tau_{s(e)}$ is shortened with increasing fluences (see Table 2), whereas $\tau_{s(e+h)}$ and $\tau_{s(h)}$ are both prolonged. This still indicates that the acoustic phonon could play important roles in the electron cooling process, while the LO phonon could dominants in the hole dynamics.[63,64] To avoid simultaneous excitation of X_A and X_B, we didn't increase the pump photon energy further. However, the excitation on the red side of the X_A band at 1.86 eV (665 nm, see Fig. S4) was also tried with the same fluence to that under 625 nm excitation. As shown in Fig. S4, no initial fast decay and rapid initial crossover shifts was observed in $D_{B(e)}$, similar to the situation encountered with pump wavelength at 640 nm. Finally, in this work, we assume that the non-radiative electron relaxation from K_{v2} to K_{v1} is much slower than that in K_c, however, the exact rate of the relaxation needs to be verified in even longer decay time range.

Conclusions

In summary, we separately distinguished the electron and hole nonequilibrium dynamics, including the initial rapid thermalization and the subsequent cooling, and concomitant many-body effects on the exciton resonances during the lowest X_A formation process at the K-valley in five-layer WS_2. Under resonant X_A excitation at 640 nm, the $D_{B(e)}$ in K_c shows a single exponential sub-ps carrier cooling process, while the $D_{A(h)}$ in K_{v1} exhibits an early sub-100fs thermalization followed by a slow sub-ps cooling process. Further to shift the pump laser spectrum to the blue side of X_A resonance at 625 nm, the $D_{B(e)}$ exhibits similar biphasic profiles to $D_{A(h)}$. The $\tau_{f(e)}$ in $D_{B(e)}$ and the $\tau_{f(h)}$ in $D_{A(h)}$ both decrease with increasing pump fluence, suggesting the process is mediated dominantly via carrier-carrier scattering. It is evidenced that the electron thermalization time has proved to be longer than that of holes. The sub-1ps cooling processes for electrons is probably dominated by acoustic phonons, whereas the holes are controlled by LO phonons. The many-body effects on exciton resonance is illustrated by first moment traces. Under resonant 640 nm excitation, both the $\langle M_{e+h}^{(1)}(t)\rangle$ and $\langle M_h^{(1)}(t)\rangle$ exhibit an initial extremely fast red- and blue-shift crossover, followed by a slow blue-shift. In contrast, the $\langle M_e^{(1)}(t)\rangle$ only includes a slow blue-shift. Also, to shift the pump to the blue side of X_A resonance at 625 nm, the hole-like dynamic behaviors, including initial fast thermalization decay in $D_{A(h)}$ and red- and blue-shift crossover in $\langle M_e^{(1)}(t)\rangle$ appear simultaneously. The extremely fast crossover could be originated from the screening of expansion of the same sign of carriers in the early time range, while the subsequent slow blue-shift is due to the net result of the competition between BGR and the effects of Pauli blocking and Coulomb screening in the cooling process. With respect to applications, firstly the observations of the separate relaxation process of electrons and holes have major implications for future optoelectronic devices based on electron or hole transport. Secondly, the analysis of many-body effects on exciton resonance is helpful to develop effective ways to dynamically control the photoelectric response of two-dimensional materials.

Conflicts of interest

There are no conflicts to declare.

Acknowledgements

This work is financially supported by the National Natural Science Foundation of China (grant Nos. 11774071 and 11704079), Science and Technology Program of Guangzhou (grant Nos. 201904010104 and 201804010451), National Natural Science Foundation of Guangdong (grant No. 501200050), State Key Laboratory of Luminescence and Applications (grant No. SKLA-2019-08), the Future Photonics Manufacturing Hub (EPSRC EP/N00762X/1) and the Chalcogenide Photonic Technologies (EPSRC EP/M008487/1) at University of Southampton, United Kingdom.

References

1 F. Withers, O. Del Pozo-Zamudio, A. Mishchenko, A. P. Rooney, A. Gholinia, K. Watanabe, T. Taniguchi, S. J. Haigh, A. K. Geim, A. I. Tartakovskii and K. S. Novoselov, *Nat. Mater.*, 2015, **14**, 301-306.
2 S. Wang, J. Wang, W. Zhao, F. Giustiniano, L. Chu, I. Verzhbitskiy, J. Zhou Yong and G. Eda, *Nano Lett.*, 2017, **17**, 5156-5162.
3 Z. Yin, H. Li, H. Li, L. Jiang, Y. Shi, Y. Sun, G. Lu, Q. Zhang, X. Chen and H. Zhang, *ACS Nano*, 2012, **6**, 74-80.
4 O. Lopez-Sanchez, D. Lembke, M. Kayci, A. Radenovic and A. Kis, *Nat. Nanotechnol.*, 2013, **8**, 497-501.
5 J. Lee, K. F. Mak and J. Shan, *Nat. Nanotechnol.*, 2016, **11**, 421-425.
6 J. R. Schaibley, H. Yu, G. Clark, P. Rivera, J. S. Ross, K. L. Seyler, W. Yao and X. Xu, *Nat. Rev. Mater.*, 2016, **1**, 16055.
7 P. Rivera, H. Yu, K. L. Seyler, N. P. Wilson, W. Yao and X. Xu, *Nat. Nanotechnol.*, 2018, **13**, 1004-1015.
8 M. Selig, F. Katsch, R. Schmidt, S. Michaelis de Vasconcellos, R. Bratschitsch, E. Malic and A. Knorr, *Phys. Rev. Res.*, 2019, **1**, 022007.
9 D. Unuchek, A. Ciarrocchi, A. Avsar, K. Watanabe, T. Taniguchi and A. Kis, *Nature*, 2018, 560, 340-344.
10 S. Wu, S. Buckley, J. R. Schaibley, L. Feng, J. Yan, D. G. Mandrus, F. Hatami, W. Yao, J. Vučković, A. Majumdar and X. Xu, *Nature*, 2015, **520**, 69-72.
11 Y. Ye, Z. J. Wong, X. Lu, X. Ni, H. Zhu, X. Chen, Y. Wang and X. Zhang, *Nat. Photonics*, 2015, **9**, 733-737.
12 K. S. Novoselov, A. Mishchenko, A. Carvalho and A. H. Castro Neto, *Science*, 2016, **353**, aac9439.
13 H. Li, X. Zheng, Y. Liu, Z. Zhang and T. Jiang, *Nanoscale*, 2018, **10**, 1650-1659.
14 Q. H. Wang, K. Kalantar-Zadeh, A. Kis, J. N. Coleman and M. S. Strano, *Nat. Nanotechnol.*, 2012, **7**, 699-712.
15 K. F. Mak, D. Xiao and J. Shan, *Nat. Photonics*, 2018, **12**, 451-460.
16 D. Y. Qiu, F. H. da Jornada and S. G. Louie, *Phys. Rev. Lett.*, 2013, **111**, 216805.
17 G. Wang, A. Chernikov, M. M. Glazov, T. F. Heinz, X. Marie, T. Amand and B. Urbaszek, *Rev. Mod. Phys.*, 2018, 90, 021001.
18 H. Wang, C. Zhang and F. *Rana, Nano Lett.*, 2015, **15**, 339-345.
19 Y. Yu, Y. Yu, C. Xu, A. Barrette, K. Gundogdu and L. Cao, *Phys. Rev. B*, 2016, **93**, 201111.
20 T. N. Lin, S. R. M. Santiago, S. P. Caigas, C. T. Yuan, T. Y. Lin, J. L. Shen and Y. F. Chen, *npj 2D Mater. and Appl.*, 2019, **3**, 46.
21 E. J. Sie, A. Steinhoff, C. Gies, C. H. Lui, Q. Ma, M. Rösner, G. Schönhoff, F. Jahnke, T. O. Wehling, Y. H. Lee, J. Kong, P. Jarillo-Herrero and N. Gedik, *Nano Lett.*, 2017, **17**, 4210-4216.
22 C. Delalande, G. Bastard, J. Orgonasi, J. A. Brum, H. W. Liu, M. Voos, G. Weimann and W. Schlapp, *Phys. Rev. Lett.*, 1987, **59**, 2690-2692.
23 B. Liu, W. Zhao, Z. Ding, I. Verzhbitskiy, L. Li, J. Lu, J. Chen, G. Eda and K. P. Loh, *Adv. Mater.*, 2016, **28**, 6457-6464.
24 D. Van Tuan, B. Scharf, Z. Wang, J. Shan, K. F. Mak, I. Žutić and H. Dery, *Phys. Rev. B*, 2019, **99**, 085301.
25 P. D. Cunningham, A. T. Hanbicki, K. M. McCreary and B. T. Jonker, *ACS Nano*, 2017, **11**, 12601-12608.
26 A. Chernikov, C. Ruppert, H. M. Hill, A. F. Rigosi and T. F. Heinz, *Nat. Photonics*, 2015, **9**, 466-470.
27 G. Wang, K. Wang, N. McEvoy, Z. Bai, C. P. Cullen, C. N. Murphy, J. B. McManus, J. J. Magan, C. M. Smith, G. S. Duesberg, I. Kaminer, J. Wang and W. J. Blau, *Small*, 2019, **15**, 1902728.
28 J. Zhao, W. Zhao, W. Du, R. Su and Q. Xiong, *Nano Res.*, 2020, **13**, 1399-1405.
29 X. Hong, J. Kim, S.-F. Shi, Y. Zhang, C. Jin, Y. Sun, S. Tongay, J.

Wu, Y. Zhang and F. Wang, *Nat. Nanotechnol.*, 2014, **9**, 682-686.
30 C. Jin, E. Y. Ma, O. Karni, E. C. Regan, F. Wang and T. F. Heinz, *Nat. Nanotechnol.*, 2018, **13**, 994-1003.
31 X. Zhu, N. R. Monahan, Z. Gong, H. Zhu, K. W. Williams and C. A. Nelson, *J. Am. Chem. Soc.*, 2015, 137, 8313-8320.
32 Y. Li, Q. Cui, F. Ceballos, S. D. Lane, Z. Qi and H. Zhao, *Nano Lett.*, 2017, **17**, 6661-6666.
33 A. F. Rigosi, H. M. Hill, Y. Li, A. Chernikov and T. F. Heinz, *Nano Lett.*, 2015, **15**, 5033-5038.
34 P. Rivera, J. R. Schaibley, A. M. Jones, J. S. Ross, S. Wu, G. Aivazian, P. Klement, K. Seyler, G. Clark, N. J. Ghimire, J. Yan, D. G. Mandrus, W. Yao and X. Xu, *Nat. Commun.*, 2015, **6**, 6242.
35 K. Wei, Y. Sui, Z. Xu, Y. Kang, J. You, Y. Tang, H. Li, Y. Ma, H. Ouyang, X. Zheng, X. Cheng and T. Jiang, *Nat. Commun.*, 2020, **11**, 3876.
36 H. Hao, Z. Xu, T. Jiang, K. Wei, H. Li, X. Zheng, K. Yin, J. You, C. Shen and X.-a. Cheng, *Opt. Express*, 2018, **26**, 15867-15886.
37 F. Ceballos, Q. Cui, M. Z. Bellus and H. Zhao, *Nanoscale*, 2016, **8**, 11681-11688.
38 Z. E. Eroglu, O. Comegys, L. S. Quintanar, N. Azam, S. Elafandi, M. Mahjouri-Samani and A. Boulesbaa, *Phys. Chem. Chem. Phys.*, 2020, **22**, 17385-17393.
39 P. Steinleitner, P. Merkl, P. Nagler, J. Mornhinweg, C. Schüller, T. Korn, A. Chernikov and R. Huber, *Nano Lett.*, 2017, 17, 1455-1460.
40 M. Breusing, S. Kuehn, T. Winzer, E. Malić, F. Milde, N. Severin, J. P. Rabe, C. Ropers, A. Knorr and T. Elsaesser, *Phys. Rev. B*, 2011, **83**, 153410.
41 Z. Nie, R. Long, L. Sun, C.-C. Huang, J. Zhang, Q. Xiong, D. W. Hewak, Z. Shen, O. V. Prezhdo and Z.-H. Loh, *ACS Nano*, 2014, **8**, 10931-10940.
42 A. Steinhoff, M. Florian, M. Rösner, G. Schönhoff, T. O. Wehling and F. Jahnke, *Nat. Commun.*, 2017, **8**, 1166.
43 H. Shi, H. Pan, Y.-W. Zhang and B. I. Yakobson, *Phys. Rev. B*, 2013, **87**, 155304.
44 T. Cheiwchanchamnangij and W. R. L. Lambrecht, *Phys. Rev. B*, 2012, **85**, 205302.
45 A. Ramasubramaniam, *Phys. Rev. B*, 2012, **86**, 115409.
46 A. Steinhoff, M. Florian, M. Rösner, M. Lorke, T. O. Wehling, C. Gies and F. Jahnke, *2D Mater.*, 2016, **3**, 031006.
47 H. Chen, Y. Li, W. Liu, H. Xu, G. Yang, J. Shi, Q. Feng, T. Yu, X. Liu and Y. Liu, *Nanoscale Horiz.*, 2018, 3, 598-605.
48 X. Liu, J. Hu, C. Yue, N. Della Fera, Y. Ling, Z. Mao and J. Wei, *ACS Nano*, 2014, **8**, 10396-10402.
49 V. Orsi Gordo, M. A. G. Balanta, Y. Galvão Gobato, F. S. Covre, H. V. A. Galeti, F. Iikawa, O. D. D. Couto, F. Qu, M. Henini, D. W. Hewak and C. C. Huang, *Nanoscale*, 2018, **10**, 4807-4815.
50 J. F. Felix, A. F. da Silva, S. W. da Silva, F. Qu, B. Qiu, J. Ren, W. M. de Azevedo, M. Henini and C.-C. Huang, *Nanoscale Horiz.*, 2020, **5**, 259-267.
51 S. Bhattacharya, A. V. Veluthandath, C. C. Huang, G. S. Murugan and P. B. Bisht, *J. Opt.*, 2020, **22**, 105003.
52 Y. Li, X. Li, T. Yu, G. Yang, H. Chen, C. Zhang, Q. Feng, J. Ma, W. Liu, H. Xu, Y. Liu and X. Liu, *Nanotechnol.*, 2018, **29**, 124001.
53 S. Schmitt-Rink, D. S. Chemla and D. A. B. Miller, Phys. Rev. B: Condens. Matter, 1985, **32**, 6601–6609.
54 F. X. Camescasse, A. Alexandrou, D. Hulin, L. Bányai, D. B. Tran Thoai and H. Haug, *Phys. Rev. Lett.*, 1996, **77**, 5429-5432.
55 A. Alexandrou, V. Berger and D. Hulin, Phys. Rev. B, 1995, 52, 4654-4657. C. Mai, A. Barrette, Y. Yu, Y. G. Semenov, K. W. Kim, L. Cao and K. Gundogdu, *Nano Lett.*, 2014, **14**, 202-206.
56 Z. Y. Zhu, Y. C. Cheng and U. Schwingenschlögl, *Phys. Rev. B*, 2011, **84**, 153402.
57 M. Montazeri, H. E. Jackson, L. M. Smith, J. M. Yarrison-Rice, J.-H. Kang, Q. Gao, H. H. Tan and C. Jagadish, *Nano Lett.*, 2012, **12**, 5389-5395.
58 B. Zhang, Z. Nie, B. Wang, D. Wang, J. Tang, X. Wang, J. Zhang, G. Xing, W. Zhang and Z. Wei, *Phys. Chem. Chem. Phys.*, 2020, **22**, 25819-25826.
59 G. Moody, J. Schaibley and X. Xu, *J. Opt. Soc. Am. B*, 2016, **33**, C39-C49.
60 P. C. Becker, H. L. Fragnito, C. H. B. Cruz, R. L. Fork, J. E. Cunningham, J. E. Henry and C. V. Shank, *Phys. Rev. Lett.*, 1988, **61**, 1647-1649.
61 J. Y. Bigot, M. T. Portella, R. W. Schoenlein, J. E. Cunningham and C. V. Shank, *Phys. Rev. Lett.*, 1991, **67**, 636-639.
62 D. Brida, A. Tomadin, C. Manzoni, Y. J. Kim, A. Lombardo, S. Milana, R. R. Nair, K. S. Novoselov, A. C. Ferrari, G. Cerullo and M. Polini, *Nat. Commun.*, 2013, **4**, 1987.
63 J. Shah, A. Pinczuk, A. C. Gossard and W. Wiegmann, *Phys. Rev. Lett.*, 1985, **54**, 2045-2048.
64 K. Kaasbjerg, K. S. Bhargavi and S. S. Kubakaddi, *Phys. Rev. B*, 2014, **90**, 165436.
65 P. D. Cunningham, K. M. McCreary and B. T. Jonker, *J. Phys. Chem. Lett.*, 2016, **7**, 5242-5246.
66 H. Dery, *Phys. Rev. B*, 2016, **94**, 075421.
67 R. E. Groenewald, M. Rösner, G. Schönhoff, S. Haas and T. O. Wehling, *Phys. Rev. B*, 2016, **93**, 205145.
68 W. T. Pollard, S. Y. Lee and R. A. Mathies, *J. Chem. Phys.*, 1990, **92**, 4012-4029.
69 N. Peyghambarian, S. W. Koch and A. Mysyrowicz, *Introduction to semiconductor optics*, Prentice Hall, Division of Simon and Schuster One Lake Street Upper Saddle River, NJ, United States, **1993**.
70 Shah, J. *Ultrafast Spectroscopy of Semiconductors and Semiconductor Nanostructures*, 2nd ed.; Springer Series in Solid-State Sciences; Springer: Berlin, **1999**.